Repository of the Max Delbrück Center for Molecular Medicine (MDC) in the Helmholtz Association

http://edoc.mdc-berlin.de/15805

Myocardial effective transverse relaxation time T2* correlates with left ventricular wall thickness: a 7.0 T MRI study

Huelnhagen, T., Hezel, F., Serradas Duarte, T., Pohlmann, A., Oezerdem, C., Flemming, B., Seeliger, E., Prothmann, M., Schulz-Menger, J., Niendorf, T.

Myocardial Effective Transverse Relaxation Time T_2^* Correlates with Left Ventricular Wall Thickness: A 7.0 T MRI Study

Till Huelnhagen[1], Fabian Hezel[1], Teresa Serradas Duarte[1], Andreas Pohlmann[1], Celal Oezerdem[1], Bert Flemming[2], Erdmann Seeliger[2], Marcel Prothmann[3,5], Jeanette Schulz-Menger[3,5], Thoralf Niendorf[1,4,5]

[1] Berlin Ultrahigh Field Facility (B.U.F.F.), Max Delbrück Center for Molecular Medicine in the Helmholtz Association, Berlin, Germany

[2] Institute of Physiology, Charité University Medicine, Berlin, Germany

[3] Working Group on Cardiovascular Magnetic Resonance, Experimental and Clinical Research Center, a joint cooperation between the Charité Medical Faculty and the Max Delbrück Center for Molecular Medicine

[4] Experimental and Clinical Research Center, a joint cooperation between the Charité Medical Faculty and the Max Delbrück Center for Molecular Medicine, Berlin, Germany

[5] DZHK (German Centre for Cardiovascular Research), partner site Berlin, Germany

Correspondence to:	Prof. Dr. Thoralf Niendorf
	Berlin Ultrahigh Field Facility (B.U.F.F.)
	Max Delbrück Center for Molecular Medicine
	Robert-Roessle-Strasse 10
	13125 Berlin
	Germany
	phone: +49 30 9406 4505
	fax: +49 30 9406 49178
	e-mail: thoralf.niendorf@mdc-berlin.de

Running title: Myocardial T_2^* correlates with myocardial wall thickness

Word count: ca. 3200
Figure count: 6

ABSTRACT

Purpose: Myocardial effective relaxation time T_2^* is commonly regarded as a surrogate for myocardial tissue oxygenation. Yet it is legitimate to assume that the factors influencing T_2^* are of multiple nature. To this end this study investigates the relationship between T_2^* and cardiac macromorphology given by left ventricular (LV) wall thickness and left ventricular radius, and provides interpretation of results in the physiological context.

Methods: High spatio-temporally resolved myocardial CINE T_2^* mapping was performed in ten healthy volunteers using a 7.0 T full body MRI system. Ventricular septal wall thickness, left ventricular inner radius and T_2^* were analyzed. Macroscopic magnetic field changes were elucidated using cardiac phase resolved magnetic field maps.

Results: Ventricular septal T_2^* changes periodically over the cardiac cycle, increasing in systole and decreasing in diastole. Ventricular septal wall thickness and T_2^* showed a significant positive correlation while inner LV radius and T_2^* were negatively correlated. The impact of macroscopic magnetic field gradients on T_2^* can be considered minor in the ventricular septum.

Conclusion: Our findings suggest that myocardial T_2^* is related to tissue blood volume fraction. Temporally resolved T_2^* mapping could be beneficial for myocardial tissue characterization and for understanding cardiac (patho)physiology in vivo.

Keywords to the abstract: magnetic resonance imaging, cardiac imaging, high field, myocardial tissue characterization, susceptibility weighted imaging, T_2^*, ultrahigh field MR

INTRODUCTION

A growing number of reports refers to mapping the effective transverse relaxation time T_2^* in basic cardiovascular magnetic resonance (CMR) research and emerging clinical CMR applications. By exploiting the blood oxygenation level-dependent (BOLD) effect (1), T_2^* sensitized CMR has been suggested as a means of assessing myocardial tissue oxygenation and perfusion. T_2^* mapping has been shown to be capable of detecting myocardial ischemia caused by a stenotic coronary artery (2), to reveal myocardial perfusion deficits under pharmacological stress (3-8), to study endothelial function (9) or to assess breathing maneuver-dependent oxygenation changes in the myocardium (10-12). In clinical application, T_2^* mapping has become the method of choice for myocardial iron quantification, an essential parameter for guiding therapy in patients with myocardial iron overload (13-17).

The rather long echo times required for sufficient T_2^* weighting together with the need for balancing the constraints dictated by cardiac and respiratory motion commonly limit application of T_2^* sensitized CMR to single cardiac phase, e.g. end diastolic, acquisitions under breath held conditions. Early animal studies investigated cardiac phase resolved BOLD signal intensity changes over the cardiac cycle (10,18) and reported differences in the BOLD signal during systole versus diastole.

The linear relationship between magnetic field strength and microscopic susceptibility effects renders the move to $B_0=7.0$ T conceptually appealing for T_2^* mapping (19-22). The enhanced susceptibility effects at 7.0 T may be useful to lower the detection level and to extend the dynamic range of the sensitivity for monitoring T_2^* changes. Transitioning to higher magnetic field strengths runs the boon that the in-phase inter-echo time governed by the fat-water phase shift is reduced from 4.8 ms (210 Hz) at 1.5 T to 1.02 ms (980 Hz) at 7.0 T. This enables rapid acquisition of multiple echoes (23) and facilitates high spatio-temporally resolved myocardial CINE T_2^* mapping of the human heart (23).

Myocardial T_2^* changes are commonly assumed to provide a surrogate for myocardial tissue oxygenation (17). Yet the factors influencing T_2^* are of multiple nature (24). Further to blood oxygenation, blood volume fraction per tissue volume, hematocrit, the oxyhemoglobin dissociation curve, main magnetic field inhomogeneities, tissue susceptibility and tissue microstructure or micromorphology were reported to govern T_2^* (25-30).

Cardiac macromorphology including ventricular radius and ventricular wall thickness constitutes another category of physiological parameters that are substantially altered throughout the cardiac cycle and might affect blood volume fraction and the amount of deoxygenated hemoglobin (deoxyHb) per tissue volume. Hence it is a legitimate hypothesis that dynamic variation in myocardial T_2^* over the cardiac cycle can be related to periodic changes in cardiac macromorphology. To test this hypothesis this note examines myocardial T_2^*, left ventricular wall thickness and left ventricular radius over the cardiac cycle in healthy subjects at 7.0 T. To meet this goal macroscopic B_0 fluctuations over the course of the cardiac cycle are analyzed first to detail its impact on T_2^*. Second, dynamic mapping of myocardial T_2^* of the left ventricle is performed using high spatio-temporally resolved CINE techniques. This is paralleled by an assessment of left ventricular radius and ventricular septal wall thickness across the cardiac cycle, which are then correlated with temporal T_2^* changes in the interventricular septum.

METHODS

Magnetic resonance hardware:

All experiments were performed on a 7.0 T whole body MR system (Magnetom, Siemens Healthcare, Erlangen, Germany, maximum gradient strength=38 mT/m, maximum slew rate=170 mT/m/ms). A 16 channel transceiver RF coil array tailored for CMR was used (31-33). An MR stethoscope (EasyACT, MRI.TOOLS GmbH, Berlin, Germany, (34-37)) and pulse oximetry were employed for cardiac triggering and gating.

B_0 shimming

To minimize the influence of macroscopic magnetic field inhomogeneities on T_2^*, B_0 shimming was carried out prior to T_2^* mapping. A B_0 field map was acquired in a single breath hold in end-diastole using an axial stack of slices covering the entire heart. A cardiac triggered multi-echo gradient-echo technique (TEs=2.04 ms and 4.08 ms, TR=5.4 ms, spatial resolution (4.2x4.2x8.0) mm^3, 18 slices) was employed. Based on this field map second order shimming was applied for a shim volume accommodating a four chamber view and a mid-ventricular short axis view of the heart.

Dynamic B_0 mapping and magnetic field simulations

To investigate temporal macroscopic field changes as a possible source of T_2^* variations over the cardiac cycle, high temporal resolution CINE B_0 maps were generated for short axis views of the heart using the first two echoes of a cardiac triggered, segmented multi-echo gradient-echo (MEGRE) technique (23,38) (spatial resolution (1.1x1.1x4.0) mm^3, flip angle 15°, TE=2.04-10.20 ms, ΔTE=1.02 ms, TR = 12.16 ms, GRAPPA (39), R=4). B_0 maps were low pass filtered to keep only macroscopic B_0 changes that vary slowly in space. In-plane B_0 gradients were calculated for each voxel as the norm of the B_0 gradients in x and y direction. Through-plane septal B_0 gradients were approximated from a line profile in the septum using end-diastolic B_0 maps covering a four chamber view of the heart (MEGRE technique, spatial resolution

(1.1x1.1x4.0) mm^3, flip angle 20°, TEs=2.04, 3.06, 5.10, 6.12 ms, TR=22.04 ms, GRAPPA R=3). Intravoxel B_0 gradients were calculated as the square root sum of squares of in-plane and through-plane B_0 gradients. An approximation of T_2^* changes induced by B_0 changes over the cardiac cycle was carried out based on the equation

$$\frac{1}{T_2^*} = \frac{1}{T_2} + \frac{1}{T_2'} = \frac{1}{T_2} + \gamma|\Delta B|$$

with γ being the gyromagnetic ratio of the proton and $|\Delta B|$ the absolute intravoxel magnetic field gradient (40,41). T_2 was assumed to be constant with regard to macroscopic field changes.

Magnetostatic field simulations were performed in MATLAB (The Mathworks, Natick, USA) (42) based on the heart of the human voxel model Duke (43) and susceptibility values for blood and tissue (44,45). Heart models with thin wall and thick wall were obtained by morphologic erosion and dilation to mimic systole and diastole. Intravoxel field gradients were calculated for a voxel size of 1x1x4 mm^3.

Dynamic myocardial T_2^* mapping

High spatial resolution CINE T_2^* mapping was performed with a segmented multi-shot multi breath hold gradient echo technique (23) using: spatial resolution (1.1x1.1x4.0) mm^3, flip angle 20°, TEs=2.04-10.20 ms, ΔTE=1.02 ms, TR=12.16 ms, GRAPPA R=4). T_2^* weighted CINE acquisitions were split in three sub-acquisitions, each acquired in one breath-hold (23). 2D CINE FLASH acquisitions (spatial resolution (1.4x1.4x4.0) mm^3, flip angle 32°, TE=2.67 ms, TR=5.66 ms, GRAPPA R=2) were used as anatomic reference. Mid-ventricular short axis views were acquired.

To investigate the effect of fat proton resonances other than methylene for echo times adjusted to fat and water being in phase, signal simulations were performed in MATLAB (The Mathworks, Natick, USA). The signal model and fat spectrum described in (46) was employed assuming a myocardial fat fraction of 3% (46,47). In-phase echo times were compared for 1.) water and only fat methylene resonances and 2.) water, fat methylene and fat methyl resonances which are the two dominant peaks in the myocardial fat spectrum (46).

Volunteer study

Ten healthy volunteers without any known history of cardiac disease (7 male, age=40.8±15.6 (mean±sd), BMI=22.8±3.2 kg/m^2) were included after due approval by the local ethical committee. Informed written consent was obtained from each volunteer prior to the study.

Data processing:

All data processing was carried out offline using customized MATLAB (The Mathworks, Natick, USA) routines. All T_2^* sensitized images were de-noised with a spatially adaptive non-local means (SANLM) filter (48,49) (VBM8 toolbox (http://dbm.neuro.uni-jena.de/vbm8/) of SPM8 (http://www.fil.ion.ucl.ac.uk/spm/)). After de-noising, the T_2^* weighted CINE images from the three breath holds were co-registered employing a non-rigid registration provided by the MIRT MATLAB toolbox (https://sites.google.com/site/myronenko/research/mirt). The image series with the shortest echo time (TE=2.04ms) was used as reference for registration. Images of the three registered scans were combined to form multi echo series covering nine echoes with increasing T_2^* weighting. Subsequently, non-linear T_2^* fitting was performed using the MATLAB trust region algorithm in combination with a mono-exponential signal decay model. Goodness-of-fit was evaluated by R^2. Additionally the fit standard deviation (T_2^*-STD) was estimated using a recently proposed method (50). Voxels with decreased fit quality (R^2 < 0.7 or T_2^*-STD > 3ms) or unnaturally high/low T_2^* (T_2^* ≤ 1 or T_2^* ≥ 50ms) were considered unreliable and excluded from further analysis.

Data analysis:

For each volunteer the left ventricular myocardium was manually segmented for all cardiac phases resulting in myocardial masks. Left ventricular wall thickness and inner radius were calculated for 2.5° wide radial segments covering the whole myocardium. This procedure was repeated for all cardiac

phases. Median T_2^* and mean wall thickness were calculated for each cardiac phase to allow assessment of temporal changes. For this purpose only anteroseptal and inferoseptal segments (51) were considered, because T_2^* measurements have been shown to be most reliable in the septum (22). Mean inner LV radius was calculated per phase by averaging over the whole ventricle to estimate wall stress as explained below. The averaged values of T_2^*, wall thickness and LV radius per cardiac phase were determined for all volunteers. Cardiac phases were normalized by division of the actual trigger times by the respective R-R interval. The number of phases was unified using linear interpolation to allow for averaging among subjects. Correlation between septal T_2^* and myocardial wall thickness was analyzed using the Pearson correlation coefficient. A *P*-value of *P* < 0.05 was considered significant. Wall stress in the left ventricular myocardium was estimated for each radial segment based on the simplified Laplace equation

$$\sigma = p \cdot \frac{r}{2 \cdot d}$$

relating transmural pressure p, inner ventricular radius r and myocardial wall thickness d to the left ventricular wall stress σ. Blood pressure was assumed constant during systole (120mmHg) and diastole (6mmHg) (52). Mean wall stress was calculated for each cardiac phase by averaging the radial segments. The cumulative frequencies of ventricular septal T_2^* in end-systole and end-diastole were calculated by summing the respective relative frequencies of T_2^* for all septal voxels in all volunteers.

RESULTS

Dynamic B_0 mapping and magnetic field simulations

Low pass filtered cardiac phase resolved B_0 maps showed very minor variation across the cardiac cycle. The mean septal intravoxel B_0 gradient was 5.3 ± 1.7 Hz/voxel over the cardiac cycle. Figure 1A shows off-center frequency maps and maps of the intravoxel B_0 gradient along the cardiac cycle for an exemplary healthy subject. The mean absolute variation of the mean intravoxel B_0 gradient in the interventricular septum over the cardiac cycle was approximately 0.4 ± 0.3 Hz/voxel. Regarding the mean observed septal T_2^* and intravoxel B_0 gradient over the cardiac cycle, the observed maximum intravoxel B_0 gradient variation translates into a T_2^* variation of approximately 0.7 ± 0.4 ms (Figure 1B).

Model based magnetostatic field simulations comparing hearts with low and high wall thickness showed only minor differences in field perturbation and intravoxel field gradients as depicted in Figure 2A. Higher wall thickness resulted in an intravoxel gradient approximately 0.5 Hz less versus low wall thickness as depicted in Figure 2B for a profile through the septum of a short axis view. This result is similar to the measured macroscopic intravoxel gradient change. A decrease of the intravoxel field gradient toward the center of the septum was observed.

Improving T_2^* mapping accuracy by spatially adaptive non local means noise filtering

SANLM filtering decreased the estimated fit standard deviation of T_2^* in the myocardium by approximately 30% in comparison to fits from unfiltered images. Figure 3 shows original but unfiltered and noise filtered magnitude images together with the corresponding T_2^* maps and T_2^* STD maps for an exemplary volunteer highlighting the decrease in noise and T_2^* standard deviation due to filtering. No artifacts due to filtering were observed in the fitted maps which is in line with previous reports on improved T_2^* fitting accuracy by non-local means filtering (49,53).

Dynamic myocardial T_2^* mapping

Figure 4A shows a series of T_2^* weighted images of a mid-ventricular short axis view of the heart to illustrate the overall image quality for the range of echo times used. Corresponding cardiac phase resolved T_2^* maps are displayed in Figure 4B as an overlay to anatomical FLASH CINE images. A T_2^* increase can be observed in systole. The septal segments revealed a transmural change of T_2^* with highest values in the center of the interventricular septum. Corresponding T_2^* fit standard deviation maps are shown in Figure 4C.

Averaged over all subjects and septal segments for all cardiac phases, mean septal wall thickness (SWT) was found to be 7.4 ± 1.6 mm. A mean T_2^*=14.2 ± 1.3 ms was obtained. For end-systole a mean SWT=9.0 ± 1.3 mm and a mean T_2^*=15.0 ± 1.4 ms were observed. For end-diastole mean SWT=5.9 ± 0.9 mm and T_2^*=13.7 ± 1.2 ms were determined. The $T_2^*{}_{systole}$/ $T_2^*{}_{diastole}$ ratio was 1.1. The mean range (max – min) of T_2^* over the cardiac cycle was 3.5 ± 1.0ms which is significantly higher (P<0.01) than the 0.7 ± 0.4 ms T_2^* change expected from the periodic macroscopic B_0 variation.

Figure 5 illustrates the relative course of mean septal wall thickness, median septal T_2^*, mean inner ventricular radius and wall stress over the cardiac cycle for all subjects. An increase of T_2^* during systole was observed, which is paralleled by an increase in the SWT and a decrease in the left-ventricular radius. In accordance to the literature myocardial wall stress increases massively during the short isovolumetric contraction phase of systole due to the pressure increase in the left ventricle, decreases slowly during the long ejection phase of the systole caused by the increase in wall thickness and decrease of inner radius, and decreases rapidly during the short isovolumetric relaxation phase of the diastole due to the left ventricular pressure drop (54-56).

The mean time courses of T_2^*, septal wall thickness and left ventricular diameter averaged over volunteers and all segments of the interventricular septum are shown in Figure 6A. End systolic T_2^* was considerably higher than end diastolic T_2^* (Figure 6B). Pearson correlation analysis yielded a significant positive correlation ($R=0.85$, $P <0.001$) of T_2^* and wall thickness (Figure 6C). For the relation between T_2^* and left ventricular radius Pearson correlation analysis provided a significant negative correlation ($R=-0.87$, $P<0.001$) as outlined in Figure 6D.

Signal simulations for the combined fat water signal revealed that the difference of in-phase echo times was less than 25μs when considering water and fat methylene resonances compared to water, fat methylene and fat methyl resonances. This yields a difference in the signal magnitudes of less than 0.2%

DISCUSSION

This study demonstrated cyclic changes of mean T_2^* over the cardiac cycle with a T_2^* increase in systole and a T_2^* decrease in diastole. This is in line with previous reports about myocardial BOLD signal intensity changes over the cardiac cycle with increased BOLD signal in systole (10,18). The main finding of our note is that the T_2^* changes show a positive correlation with myocardial wall thickness and a negative correlation with left ventricular radius.

To exclude macroscopic field fluctuations as a possible source of cyclic T_2^* changes, macroscopic B_0 variation was elucidated over the cardiac cycle. The minor variations of septal intravoxel B_0 gradients detected over the cardiac cycle indicate that the temporal variations in T_2^* do not result from macroscopic B_0 changes. This accords with a previous study at 1.5 T reporting only minor B_0 fluctuations over the cardiac cycle (57), and provides encouragement that such fluctuations are not a concern even at ultrahigh fields.

We suppose that the observed T_2^* variation is caused by physiological changes such as perfusion and tissue oxygenation as suggested by Yablonskiy et al who related T_2^* to hematocrit, blood volume fraction and blood oxygenation (41). If T_2^* is interpreted to reflect tissue oxygenation, the observed systolic T_2^* increase would imply an increase in left myocardial oxygenation during systole, which is contrary to physiological knowledge. The contraction of the myocardium compresses the intramyocardial vasculature such that inflow of arterial blood ceases while deoxygenized blood is squeezed out of the myocardium toward the venous coronary sinus (55,56,58). Meanwhile the myocytes continue to consume oxygen (55,58) resulting in a higher fraction of deoxygenized hemoglobin (lower O_2-saturation of Hb; SpO_2) which should result in a T_2^* decrease. However, the major decrease in blood volume fraction of the myocardium reduces the amount of deoxygenized blood per tissue volume, thereby

increasing instead of lowering T_2^* during systole. The short continuation of the increase in T_2^* during the beginning of diastole which was observed in some volunteers could be caused by the oxygen rich blood flowing into the myocardium.

We found a positive correlation of wall thickness and T_2^* and a negative correlation between LV radius and T_2^*. According to Laplace's equation, wall thickness, LV radius, and intraventricular pressure determine wall stress. Our results on the time course of wall thickness, LV radius, and wall stress throughout the cardiac cycle agree with data obtained by invasive techniques in dogs, in which LV pressure was additionally recorded (54). The steep rise in wall stress during the short isovolumetric contraction phase of the systole results from the manifold pressure increase that also reduces the myocardial blood volume fraction. The mild and slow decrease in wall stress during the ejection phase relies on the shortening of the myocardium that simultaneously decreases the radius and increases the wall thickness. With the onset of the diastole, isovolumetric relaxation results in immediate pressure drop and thus a steep decline in wall stress. The induced increase in myocardial perfusion results in a higher myocardial blood volume fraction and consequently stronger influence of deoxyhemoglobin on T_2^*. The observed changes in T_2^* over the cardiac cycle are therefore likely driven by myocardial blood volume fraction changes dominated by the high pressure difference between diastole and systole.

Another possible confounder could be a more uniform mesoscopic magnetic field and hence reduced spin dephasing for higher wall thickness due to a more homogenous susceptibility distribution. This could also explain the observed transmural T_2^* change in septal areas with highest T_2^* in the center between endo- and epicardium and thus farthest away from susceptibility transitions between blood and tissue. To investigate this possibility, basic magnetostatic field simulations were performed for heart models with low and high wall thickness to mimic systole and diastole. The simulation results indicate

that the intravoxel field gradient resulting from the static field is indeed declining toward the center of the septum, but the difference in the field gradient for low and high wall thickness is rather low and not sufficient to explain the observed T_2^* difference between systole and diastole.

Signal simulations performed to investigate the impact of fat resonances other than methylene for T_2^* mapping indicate that it is sufficient to account for methylene resonances for the choice of echo times at which fat and water are in phase in the healthy myocardium.

CONCLUSIONS

Interventricular septal myocardial T_2^* changes periodically during the cardiac cycle in healthy volunteers. It increases in systole and decreases in diastole. Ventricular septal wall thickness and T_2^* show a significant positive correlation. The observed cyclic T_2^* variations are likely related to changes in myocardial blood volume fraction throughout the cardiac cycle. The underlying biophysical and/or physiological mechanisms causing the T_2^* changes warrant further investigation. The SWT and T_2^* relationship bears the potential for myocardial tissue characterization and for better understanding cardiac (patho)physiology in vivo..

ACKNOWLEDGEMENT

REFERENCES

1. Ogawa S, Menon RS, Tank DW, Kim SG, Merkle H, Ellermann JM, Ugurbil K. Functional brain mapping by blood oxygenation level-dependent contrast magnetic resonance imaging. A comparison of signal characteristics with a biophysical model. Biophys J. 1993;64:803-812.

2. Wacker CM, Hartlep AW, Pfleger S, Schad LR, Ertl G, Bauer WR. Susceptibility-sensitive magnetic resonance imaging detects human myocardium supplied by a stenotic coronary artery without a contrast agent. J Am Coll Cardiol. 2003;41:834-840.

3. Friedrich M, Niendorf T, Schulz-Menger J. Blood oxygen level-dependent magnetic resonance imaging in patients with stress-induced angina. ACC Current Journal Review. 2004;13:30.

4. Jahnke C, Gebker R, Manka R, Schnackenburg B, Fleck E, Paetsch I. Navigator-gated 3D blood oxygen level–dependent CMR at 3.0-T for detection of stress-induced myocardial ischemic reactions. JACC: Cardiovascular Imaging. 2010;3:375-384.

5. Karamitsos TD, Leccisotti L, Arnold JR, Recio-Mayoral A, Bhamra-Ariza P, Howells RK, Searle N, Robson MD, Rimoldi OE, Camici PG. Relationship Between Regional Myocardial Oxygenation and Perfusion in Patients With Coronary Artery Disease Insights From Cardiovascular Magnetic Resonance and Positron Emission Tomography. Circulation: Cardiovascular Imaging. 2010;3:32-40.

6. Tsaftaris SA, Tang R, Zhou X, Li D, Dharmakumar R. Ischemic extent as a biomarker for characterizing severity of coronary artery stenosis with blood oxygen-sensitive MRI. Journal of magnetic resonance imaging. 2012;35:1338-1348.

7. Wacker CM, Bock M, Hartlep AW, Beck G, van Kaick G, Ertl G, Bauer WR, Schad LR. Changes in myocardial oxygenation and perfusion under pharmacological stress with dipyridamole: assessment using T*2 and T1 measurements. Magn Reson Med. 1999;41:686-695.

8. Vohringer M, Flewitt JA, Green JD, Dharmakumar R, Wang J, Jr., Tyberg JV, Friedrich MG. Oxygenation-sensitive CMR for assessing vasodilator-induced changes of myocardial oxygenation. J Cardiovasc Magn Reson. 2010;12:20.

9. Utz W, Jordan J, Niendorf T, Stoffels M, Luft FC, Dietz R, Friedrich MG. Blood oxygen level-dependent MRI of tissue oxygenation: relation to endothelium-dependent and endothelium-independent blood flow changes. Arterioscler Thromb Vasc Biol. 2005;25:1408-1413.

10. Guensch DP, Fischer K, Flewitt JA, Friedrich MG. Impact of intermittent apnea on myocardial tissue oxygenation–a study using oxygenation-sensitive cardiovascular magnetic resonance. PLoS One. 2013;8:e53282.

11. Guensch DP, Fischer K, Flewitt JA, Friedrich MG. Myocardial oxygenation is maintained during hypoxia when combined with apnea–a cardiovascular MR study. Physiological reports. 2013;1:e00098.

12. Guensch DP, Fischer K, Flewitt JA, Yu J, Lukic R, Friedrich JA, Friedrich MG. Breathing manoeuvre-dependent changes in myocardial oxygenation in healthy humans. Eur Heart J Cardiovasc Imaging. 2014;15:409-414.

13. He T. Cardiovascular magnetic resonance T2* for tissue iron assessment in the heart. Quant Imaging Med Surg. 2014;4:407-412.

14. Anderson L, Holden S, Davis B, Prescott E, Charrier C, Bunce N, Firmin D, Wonke B, Porter J, Walker J. Cardiovascular T 2-star(T 2*) magnetic resonance for the early diagnosis of myocardial iron overload. European Heart Journal. 2001;22:2171-2179.

15. Mavrogeni S. Evaluation of myocardial iron overload using magnetic resonance imaging. Blood Transfusion. 2009;7:183.

16. Carpenter J-P, He T, Kirk P, Roughton M, Anderson LJ, de Noronha SV, Sheppard MN, Porter JB, Walker JM, Wood JC. On T2* magnetic resonance and cardiac iron. Circulation. 2011;123:1519-1528.

17. Friedrich MG, Karamitsos TD. Oxygenation-sensitive cardiovascular magnetic resonance. J Cardiovasc Magn Reson. 2013;15:43.

18. Tsaftaris SA, Zhou X, Tang R, Li D, Dharmakumar R. Detecting myocardial ischemia at rest with cardiac phase-resolved blood oxygen level-dependent cardiovascular magnetic resonance. Circ Cardiovasc Imaging. 2013;6:311-319.

19. Turner R, Jezzard P, Wen H, Kwong KK, Le Bihan D, Zeffiro T, Balaban RS. Functional mapping of the human visual cortex at 4 and 1.5 tesla using deoxygenation contrast EPI. Magn Reson Med. 1993;29:277-279.

20. van der Zwaag W, Francis S, Head K, Peters A, Gowland P, Morris P, Bowtell R. fMRI at 1.5, 3 and 7 T: characterising BOLD signal changes. Neuroimage. 2009;47:1425-1434.

21. Donahue MJ, Hoogduin H, van Zijl PC, Jezzard P, Luijten PR, Hendrikse J. Blood oxygenation level-dependent (BOLD) total and extravascular signal changes and DeltaR2* in human visual cortex at 1.5, 3.0 and 7.0 T. NMR Biomed. 2011;24:25-34.

22. Meloni A, Hezel F, Positano V, Keilberg P, Pepe A, Lombardi M, Niendorf T. Detailing magnetic field strength dependence and segmental artifact distribution of myocardial effective transverse relaxation rate at 1.5, 3.0, and 7.0 T. Magn Reson Med. 2014;71:2224-2230.

23. Hezel F, Thalhammer C, Waiczies S, Schulz-Menger J, Niendorf T. High spatial resolution and temporally resolved T2* mapping of normal human myocardium at 7.0 Tesla: an ultrahigh field magnetic resonance feasibility study. PLoS One. 2012;7:e52324.

24. Niendorf T, Pohlmann A, Arakelyan K, et al. How bold is blood oxygenation level-dependent (BOLD) magnetic resonance imaging of the kidney? Opportunities, challenges and future directions. Acta Physiol (Oxf). 2015;213:19-38.

25. Christen T, Zaharchuk G, Pannetier N, Serduc R, Joudiou N, Vial JC, Remy C, Barbier EL. Quantitative MR estimates of blood oxygenation based on T2*: a numerical study of the impact of model assumptions. Magn Reson Med. 2012;67:1458-1468.

26. Lee J, van Gelderen P, Kuo LW, Merkle H, Silva AC, Duyn JH. T2*-based fiber orientation mapping. Neuroimage. 2011;57:225-234.

27. Dibb R, Qi Y, Liu C. Magnetic susceptibility anisotropy of myocardium imaged by cardiovascular magnetic resonance reflects the anisotropy of myocardial filament alpha-helix polypeptide bonds. J Cardiovasc Magn Reson. 2015;17:60.

28. Li TQ, van Gelderen P, Merkle H, Talagala L, Koretsky AP, Duyn J. Extensive heterogeneity in white matter intensity in high-resolution T2*-weighted MRI of the human brain at 7.0 T. Neuroimage. 2006;32:1032-1040.

29. Shmueli K, de Zwart JA, van Gelderen P, Li TQ, Dodd SJ, Duyn JH. Magnetic susceptibility mapping of brain tissue in vivo using MRI phase data. Magn Reson Med. 2009;62:1510-1522.

30. Ziener CH, Kampf T, Melkus G, Jakob PM, Schlemmer HP, Bauer WR. Signal evolution in the local magnetic field of a capillary - analogy to the damped driven harmonic oscillator. Magn Reson Imaging. 2012;30:540-553.

31. Thalhammer C, Renz W, Winter L, et al. Two-dimensional sixteen channel transmit/receive coil array for cardiac MRI at 7.0 T: design, evaluation, and application. J Magn Reson Imaging. 2012;36:847-857.

32. Winter L, Kellman P, Renz W, Grassl A, Hezel F, Thalhammer C, von Knobelsdorff-Brenkenhoff F, Tkachenko V, Schulz-Menger J, Niendorf T. Comparison of three multichannel transmit/receive radiofrequency coil configurations for anatomic and functional cardiac MRI at 7.0T: implications for clinical imaging. Eur Radiol. 2012;22:2211-2220.

33. Prothmann M, von Knobelsdorff-Brenkenhoff F, Töpper A, Dieringer MA, Shahid E, Graessl A, Rieger J, Lysiak D, Thalhammer C, Huelnhagen T. High Spatial Resolution Cardiovascular Magnetic Resonance at

7.0 Tesla in Patients with Hypertrophic Cardiomyopathy–First Experiences: Lesson Learned from 7.0 Tesla. PLoS One. 2016;11:e0148066.

34. Frauenrath T, Hezel F, Renz W, d'Orth Tde G, Dieringer M, von Knobelsdorff-Brenkenhoff F, Prothmann M, Schulz Menger J, Niendorf T. Acoustic cardiac triggering: a practical solution for synchronization and gating of cardiovascular magnetic resonance at 7 Tesla. J Cardiovasc Magn Reson. 2010;12:67.

35. Frauenrath T, Hezel F, Heinrichs U, Kozerke S, Utting JF, Kob M, Butenweg C, Boesiger P, Niendorf T. Feasibility of cardiac gating free of interference with electro-magnetic fields at 1.5 Tesla, 3.0 Tesla and 7.0 Tesla using an MR-stethoscope. Invest Radiol. 2009;44:539-547.

36. Frauenrath T, Niendorf T, Kob M. Acoustic method for synchronization of Magnetic Resonance Imaging (MRI). Acta Acustica united with Acustica. 2008:148-155.

37. Becker M, Frauenrath T, Hezel F, et al. Comparison of left ventricular function assessment using phonocardiogram- and electrocardiogram-triggered 2D SSFP CINE MR imaging at 1.5 T and 3.0 T. Eur Radiol. 2010;20:1344-1355.

38. Haacke EM, Brown RW, Thompson MR, Venkatesan R. Segmented k-Space: Phase Encoding Multiple k-Space Lines per RF Excitation for Gradient Echo Imaging. In: Magnetic Resonance Imaging - Physical Principles and Sequence Design. 1 ed: John Wiley & Sons; 1999. p 516-524.

39. Griswold MA, Jakob PM, Heidemann RM, Nittka M, Jellus V, Wang J, Kiefer B, Haase A. Generalized autocalibrating partially parallel acquisitions (GRAPPA). Magn Reson Med. 2002;47:1202-1210.

40. Haacke EM, Brown RW, Thompson MR, Venkatesan R. Magnetic Field Inmhomogeneity Effects and T2* Dephasing. In: Magnetic Resonance Imaging - Physical Principles and Sequence Design. 1 ed: John Wiley & Sons; 1999. p 569-617.

41. Yablonskiy DA, Haacke EM. Theory of NMR signal behavior in magnetically inhomogeneous tissues: the static dephasing regime. Magn Reson Med. 1994;32:749-763.
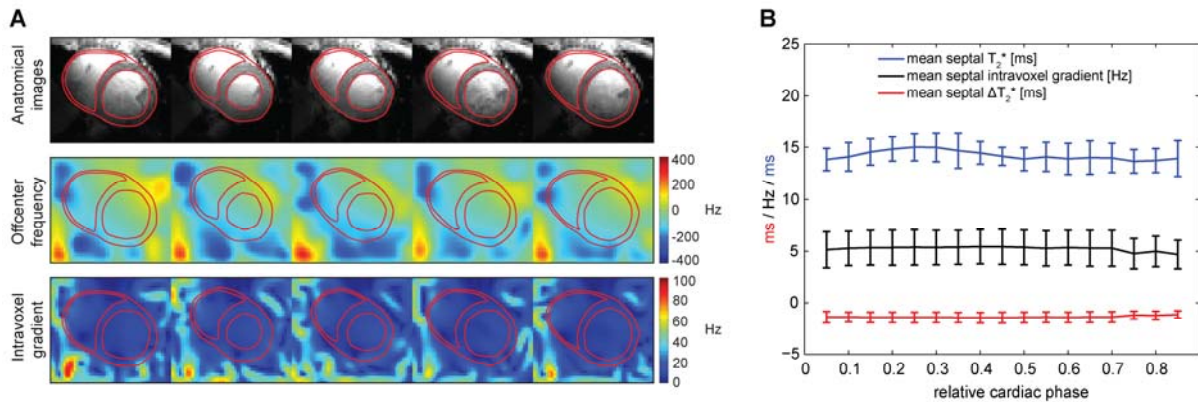
42. Salomir R, de Senneville BD, Moonen CTW. A fast calculation method for magnetic field inhomogeneity due to an arbitrary distribution of bulk susceptibility. Concepts in Magnetic Resonance Part B: Magnetic Resonance Engineering. 2003;19B:26-34.

43. Christ A, Kainz W, Hahn EG, Honegger K, Zefferer M, Neufeld E, Rascher W, Janka R, Bautz W, Chen J. The Virtual Family—development of surface-based anatomical models of two adults and two children for dosimetric simulations. Phys Med Biol. 2009;55:N23.

44. Schenk JF. The role of magnetic susceptibility in magnetic resonance imaging: MRI magnetic compatibility of the first and second kinds. Medical Physics. 1996;23:815-850.

45. Spees WM, Yablonskiy DA, Oswood MC, Ackerman JJ. Water Proton MR Properties of Human Blood at 1.5 Tesla: Magnetic Susceptibility, T1, T2, T2*, and Non-Lorentzian Signal Behavior. Magn Reson Med. 2001;45:533-542.

46. Venkatesh BA, Lima JA, Bluemke DA, Lai S, Steenbergen C, Liu C-Y. MR proton spectroscopy for myocardial lipid deposition quantification: a quantitative comparison between 1.5 T and 3T. Journal of Magnetic Resonance Imaging. 2012;36:1222-1230.

47. Liu CY, Redheuil A, Ouwerkerk R, Lima JA, Bluemke DA. Myocardial fat quantification in humans: evaluation by two-point water-fat imaging and localized proton spectroscopy. Magn Reson Med. 2010;63:892-901.

48. Manjon JV, Coupe P, Marti-Bonmati L, Collins DL, Robles M. Adaptive non-local means denoising of MR images with spatially varying noise levels. Journal of Magnetic Resonance Imaging. 2010;31:192-203.

49. Feng Y, He T, Feng M, Carpenter JP, Greiser A, Xin X, Chen W, Pennell DJ, Yang GZ, Firmin DN. Improved pixel-by-pixel MRI R2* relaxometry by nonlocal means. Magn Reson Med. 2014;72:260-268.

50. Sandino CM, Kellman P, Arai AE, Hansen MS, Xue H. Myocardial T2* mapping: influence of noise on accuracy and precision. J Cardiovasc Magn Reson. 2015;17:7.

51. Cerqueira MD, Weissman NJ, Dilsizian V, Jacobs AK, Kaul S, Laskey WK, Pennell DJ, Rumberger JA, Ryan T, Verani MS. Standardized myocardial segmentation and nomenclature for tomographic imaging of the heart: a statement for healthcare professionals from the Cardiac Imaging Committee of the Council on Clinical Cardiology of the American Heart Association. Circulation. 2002;105:539-542.

52. Guyton AC, Hall JE. Heart Muscle; The Heart as a Pump. In: Guyton and Hall textbook of medical physiology. 10 ed. Philadelphia: Saunders; 2000. p 96-106.

53. Huelnhagen T, Pohlmann A, Niendorf T. Improving T2* mapping accuracy by spatially adaptive non local means noise filtering. Proc Intl Soc Mag Reson Med 23; 2015; Toronto, Canada. p 3753.

54. DeAnda A, Komeda M, Moon MR, Green GR, Bolger AF, Nikolic SD, Daughters GT, Miller DC. Estimation of regional left ventricular wall stresses in intact canine hearts. American Journal of Physiology-Heart and Circulatory Physiology. 1998;275:H1879-H1885.

55. Guyton AC, Hall JE. Muscle blood flow and cardiac output during exercise; the coronary circulation and ischemic heart disease. In: Guyton and Hall textbook of medical physiology. 10 ed. Philadelphia: Saunders; 2000. p 223-234.

56. Schmidt RF, Lang F, Heckmann M. Herzmechanik. In: Physiologie des Menschen: mit Pathophysiologie. 31 ed. Heidelberg: Springer; 2010. p 539-564.

57. Shah S, Kellman P, Greiser A, Weale PJ, Zuehlsdorff S, Jerecic R. Rapid Fieldmap Estimation for Cardiac Shimming. Intl Soc Mag Reson Med 17; 2009; Hawai, USA. p 565.

58. Schmidt RF, Lang F, Heckmann M. Herzstoffwechsel und Kroronardurchblutung. In: Physiologie des Menschen: mit Pathophysiologie. 31 ed. Heidelberg: Springer; 2010. p 565-571.
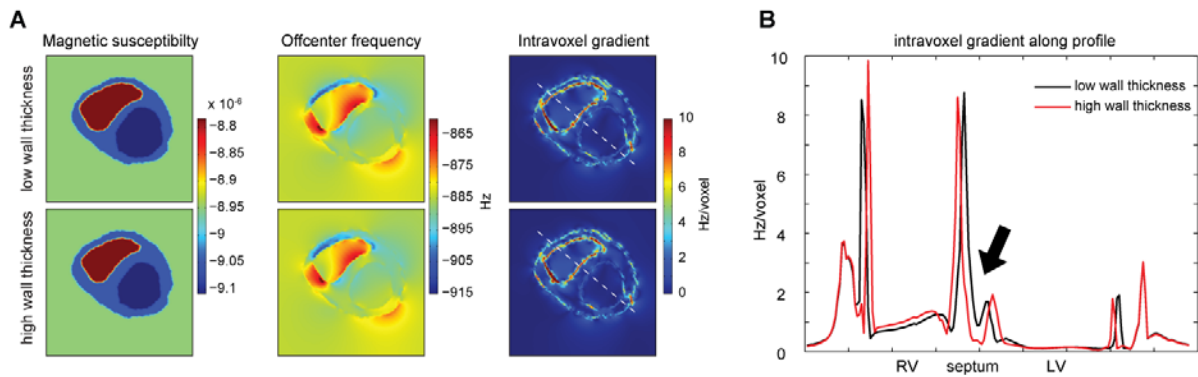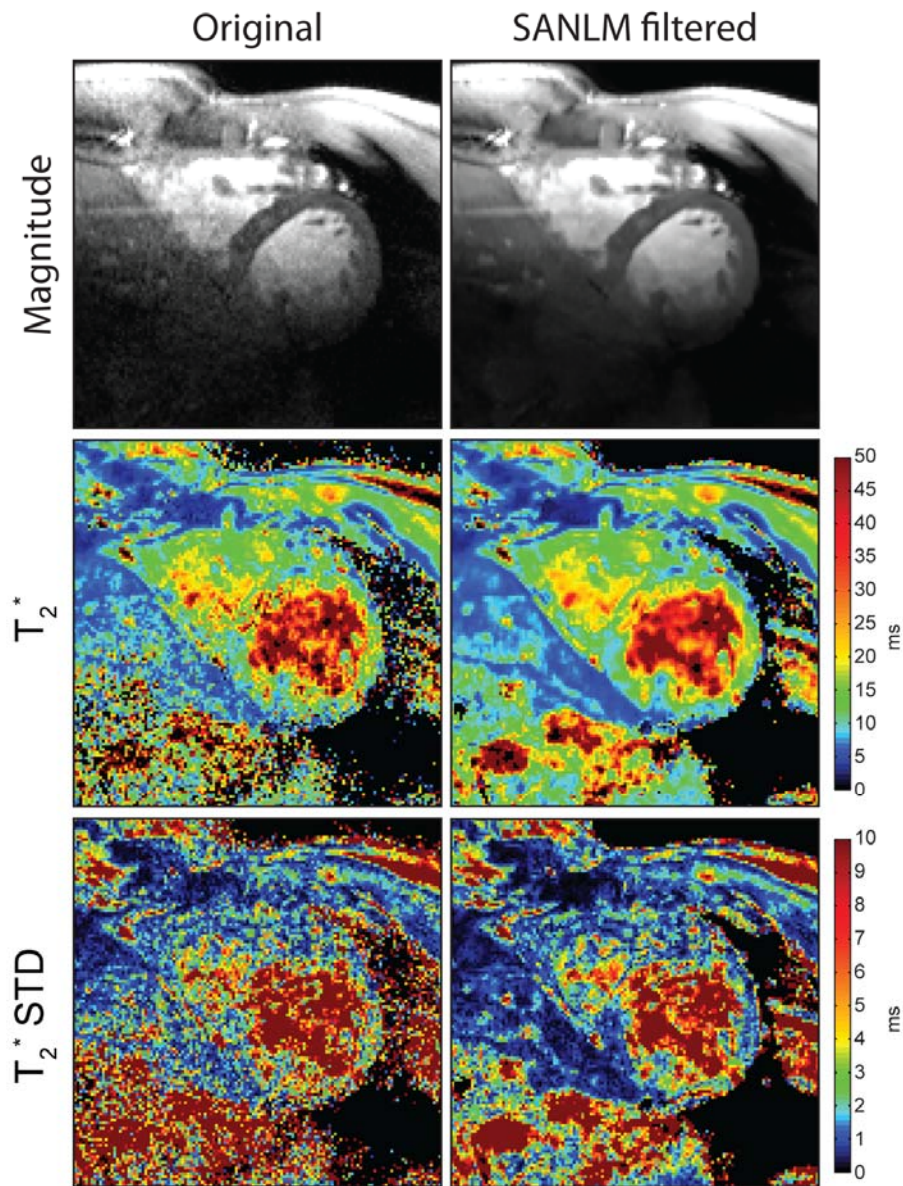
Figures

Figure 1:

B_0 field and intravoxel gradient over the cardiac cycle which were derived from a short axis view of heart of a healthy subject. **A) Top:** Anatomical magnitude images. **Center:** low pass filtered offcenter frequency maps. **Bottom:** intravoxel field gradient maps, **B)** plot of mean intravoxel B_0 gradient (black) in the left ventricular myocardium over the cardiac cycle. Relative cardiac phase 0 indicates the beginning of systole. The estimated T_2^* shift caused by the B_0 variation assuming a common myocardial T_2^* value at 7.0 T of 15ms is shown in red. Macroscopic myocardial B_0 gradient variations over the cardiac cycle can be considered minor regarding their effects on T_2^*. Error bars indicate SD.
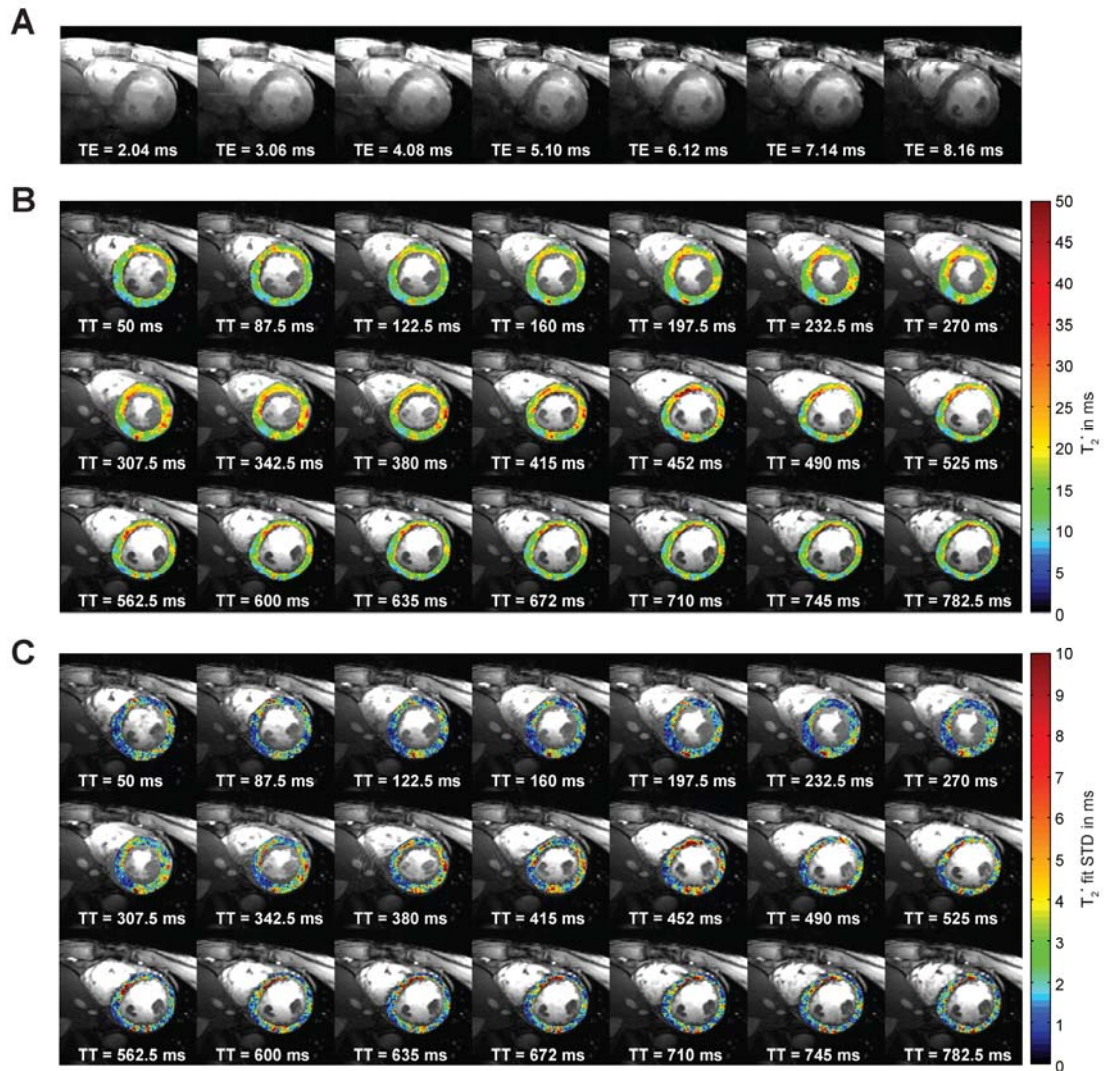
Figure 2:

Analysis of the impact of myocardial wall thickness on the macroscopic magnetic field. **A)** Short axis view obtained from magnetostatic field simulations for low and high myocardial wall thickness that mimic systole and diastole. **Left:** Model of magnetic susceptibility, **center:** Off-resonance frequency, **right:** Intravoxel field gradient. **B)** Intravoxel gradient for low and high wall thickness along a profile through the septum shown in A, demonstrating similar curves for both cases. A decrease of the field gradient can be observed toward the center of the septum indicated by the black arrow.
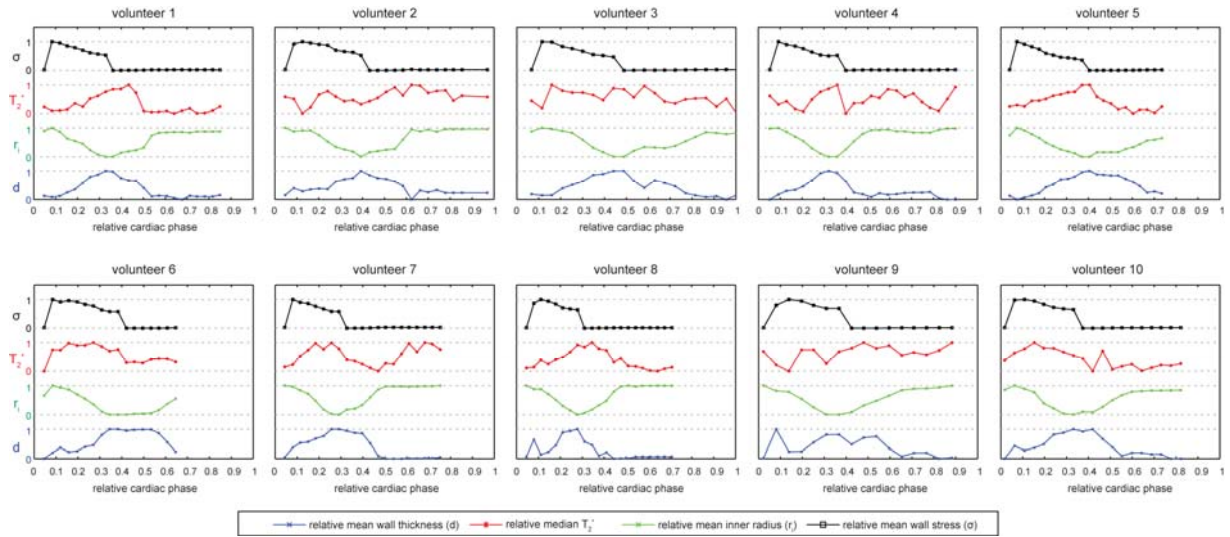
Impact of SANLM noise filtering on T_2^* maps of a mid-ventricular short axis view of the heart. **Top:** Original and SANLM filtered signal magnitude images of the first echo (TE=2.04ms) of a series of multi-echo gradient echo images. **Center:** Corresponding T_2^* maps in ms. **Bottom:** T_2^* standard deviation map illustrating the precision of the T_2^* maps. By applying the noise filter, an average decrease in T_2^* standard deviation of about 30 % in the left ventricular myocardium was achieved.
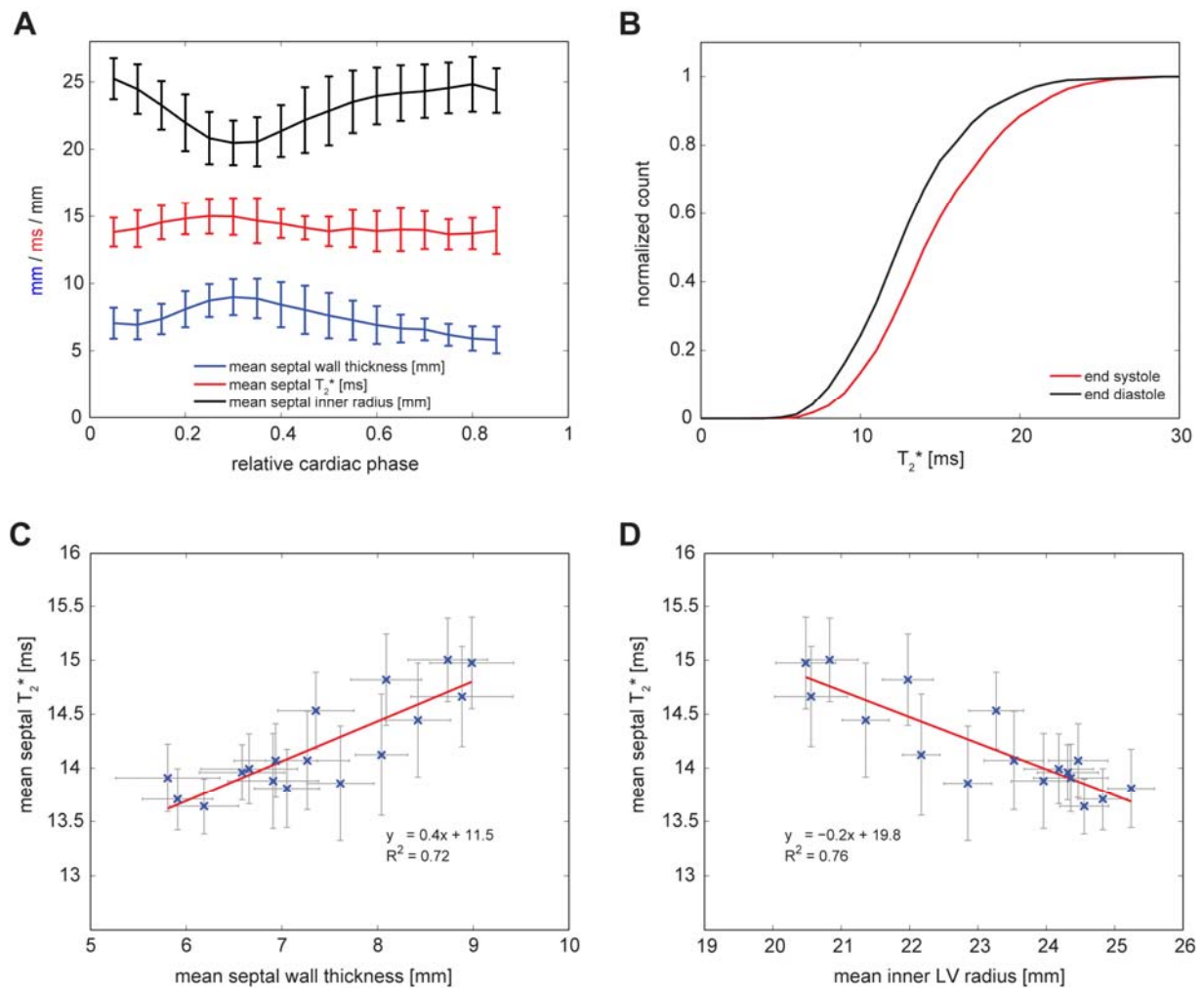
Figure 4:

High spatio-temporally resolved T_2^* mapping of a mid-ventricular short axis view of the heart of a healthy volunteer. **A:** Signal magnitude images of one cardiac phase for increasing echo times illustrating overall imaging quality and T_2^* induced signal decay. **B:** High spatial resolution cardiac phase resolved myocardial T_2^* maps (spatial resolution: 1.1x1.1x4.0mm) of a healthy volunteer at 7.0 T overlaid on FLASH CINE images. Distinct T_2^* changes can be observed in the myocardium over the cardiac cycle. **C:** Corresponding map of the T_2^* fit standard deviation. Please note the different color scales. TT indicates time to trigger.

Figure 5:

Normalized plots of mean septal wall stress (σ), T_2^*, wall thickness (d) and inner left ventricular radius (r_i) plotted over the cardiac cycle for all ten volunteers. For easier comparability, cardiac phases were referenced to their relative position in the cardiac cycle by dividing the respective time to trigger by the R-R interval. Phase 0 indicates the beginning of systole. Additionally all parameters were normalized to the same range from 0 to 1. Clear similarities in the time courses can be observed for wall thickness and T_2^* in most volunteers.

Figure 6:

Relationship of septal myocardial wall thickness, T_2^* and LV inner radius in healthy volunteers at 7.0 T **A)** course of mean septal wall thickness, mean LV inner radius and mean septal T_2^* plotted over the cardiac cycle averaged for all volunteers. Error bars indicate SD. **B)** Cumulative frequency plot of ventricular septal T_2^* in end-systole and end-diastole for all septal voxels of all volunteers. A clear shift to higher T_2^* in systole can be recognized. **C)** Scatter plot of mean septal T_2^* over mean septal wall thickness in healthy volunteers. **D)** Scatter plot of mean septal T_2^* over mean septal inner LV radius. A clear correlation can be observed for both septal wall thickness and inner radius to septal T_2^*. Error bars in scatter plots indicate SEM.